

1 **Depth-dependent crustal stress rotation and strength variation in the Charlevoix Seismic**
2 **Zone (CSZ), Québec, Canada**

3

4 A. Verdecchia¹, J. Onwuemeka², Y. Liu², and R. M. Harrington¹

5 ¹Institute of Geology, Mineralogy and Geophysics, Ruhr-University Bochum, Bochum,
6 Germany.

7 ²Department of Earth and Planetary Sciences, McGill University, Montreal, Québec, Canada.

8

9 Corresponding author: Alessandro Verdecchia (alessandro.verdecchia@rub.de)

10 **Key Points:**

- 11 • Preexisting weaknesses in the CSZ amplify postglacial horizontal stresses and cause large
12 clockwise stress rotations
- 13 • Stress rotation is further amplified in mid-crust due to low friction and semi-brittle
14 behavior
- 15 • The frequency-magnitude distribution of earthquakes suggests an inverse relationship of
16 *b*-value with differential stress in the upper crust

17

18 **Abstract**

19 Intraplate tectonic stress fields are complex due to the imprint of a long geological history. Here
20 we use a new dataset of earthquake focal mechanism solutions and relocated events to
21 investigate the relationship between regional stress, crustal strength, and seismicity in the
22 Charlevoix Seismic Zone (CSZ), the most active seismic zone in eastern Canada. Our stress
23 inversion shows that S_{Hmax} gradually rotates clockwise from approximately St. Lawrence River-

24 parallel near the surface to river-perpendicular in the lower crust, as postglacial rebound stress
25 becomes increasingly dominant at greater depth. The stress rotation occurs primarily between
26 ~13 and ~26 km depth, where glacial rebound induced stress perturbation is further amplified by
27 a “weaker” middle crust of an estimated apparent friction coefficient of ~0.5. Finally, depth-
28 dependent b -values confirm the rheological difference between upper and middle crust in the
29 CSZ.

30

31 **Plain Language Summary**

32 The occurrence of earthquakes in continent interiors is controlled by several geological and
33 geophysical conditions which are often poorly known. High-resolution earthquake catalogs and
34 information about faulting mechanisms are therefore key for recognizing and quantifying the
35 crustal stress and strength conditions in these challenging regions. This study focuses on the
36 Charlevoix Seismic Zone (CSZ), one of the most seismically active regions in eastern North
37 America. By analyzing a new set of earthquake distribution and faulting data, we found that the
38 combination between a “weak” fault zone and crustal stresses generated by postglacial rebound
39 possibly controls the spatio-temporal distribution of earthquakes in the CSZ. In particular, the
40 seismicity rate and faulting style in the CSZ strongly relate with the depth-dependent frictional
41 and rheological properties of the crust.

42

43 **1. Introduction**

44 Crustal stress magnitude and orientation exhibits primary control on fault slip and earthquake
45 rupture behavior. Because direct *in situ* stresses measurements are challenging and often
46 restricted to the shallowest part of the upper crust, regional stress field orientation is typically

47 inferred by indirect estimation, particularly at seismogenic depths. Stress inversion based on
48 earthquake focal mechanism solutions (FMS) provide a robust tool to quantify the spatio-
49 temporal distribution of stress orientation and relative magnitudes that are critical for studying
50 the source mechanisms of plate boundary and intraplate seismicity (e.g., Hardebeck & Hauksson,
51 2001; Mazzotti & Townend, 2010). Moreover, results from stress inversions can be evaluated
52 against the frequency-magnitude distribution of earthquakes to better understand the relationship
53 between seismic activity, stress orientation, and crustal strength (Abolfathian et al., 2019). For
54 example, *b*-values exhibit spatio-temporal variations that may be indicative of spatio-temporal
55 changes in stress. Van Stiphout et al. (2009) found that higher *b*-value is associated with slab
56 dehydration in the Alaskan subduction zone, which leads to pore pressure increases and
57 subsequent fault strength reduction that promotes failure. Mori & Abercrombie (1997) studied
58 the influence of earthquake hypocenters between 0 and 13 km from various dataset (**M** 2.0 - 5.5)
59 in northern and southern in California, and found that decreasing heterogeneity in crustal
60 materials with depth leads to *b*-value decreases. They interpreted rupture growth increases with
61 lithostatic stress and decreasing heterogeneity to lead to an increase in propensity of larger
62 earthquakes with depth as the crust becomes more homogeneous.

63

64 Intraplate tectonic settings pose specific challenges for quantifying crustal stress and strength
65 conditions and their relation to earthquakes. In general, the relatively lower intraplate seismicity
66 rates provide limited information about the geological and geophysical conditions for generating
67 earthquakes, such as well-constrained earthquake rates or potential maximum magnitudes, which
68 are key parameters for hazard assessment (Stein & Mazzotti, 2007 and references therein).
69 Nevertheless, intraplate settings can experience infrequent, destructive earthquakes. The

70 Charlevoix Seismic Zone (CSZ) (Figure 1) along the St. Lawrence paleorift system in eastern
71 Canada is one of the most seismically active intraplate settings, and has experienced five **M** 6+
72 earthquakes since the seventeenth century (Adams & Basham, 1991; Lamontagne, 1987),
73 including a **M** 7.3 to 7.9 in Charlevoix in 1663 (Ebel, 2011). Structural inheritance related to the
74 Grenville and Taconian orogeny, the coincident breakup of Rodinia and opening of the Iapetus
75 Ocean, and late Ordovician to early Silurian meteorite impact causes extensive lithospheric-scale
76 tectonic weakness within the paleorift system (Lemieux et al., 2003; Mazzotti & Gueydan, 2018;
77 Rondot, 1971; Schmieder et al., 2019). The rifting associated with the Iapetus Ocean opening
78 created the St. Lawrence valley system of normal faults that are presently under compressional
79 stress conditions (Adams & Basham, 1991; Johnston, 1989). Seismic tomography and
80 gravitational field modeling suggest that seismic velocity variations are dominated by the
81 distribution of crustal fractures within the impact structure and material composition outside the
82 impact structure. The crustal characteristics dictate distinctive spatial distributions of earthquake
83 source properties, such as magnitudes, focal mechanisms, and static stress drop values
84 (Onwuemeka et al., 2018; 2021). Postglacial rebound associated with glacial retreat following
85 the Wisconsin glaciation (85 – 11 kyr) superimposes ambient stresses which possibly contribute
86 to stress perturbations on critically stressed faults in the CSZ (Quinlan, 1984; Wu & Hasegawa,
87 1996). In particular, Mazzotti & Townend (2010) hypothesize that postglacial rebound in
88 combination with a weak fault zone may explain the ~30° clockwise rotation of the maximum
89 horizontal stress from shallow borehole measurements to those inferred from CSZ earthquake
90 FM solutions. While the FMS-inferred stress orientations by Mazzotti & Townend (2010) may
91 be representative of the entire region, the limited number of solutions (60) from their study make
92 it difficult to estimate possible spatial variation of the stress orientation. In particular, depth-

93 dependent stress variation would provide critical insights for understanding the rheological
94 properties of the lithosphere, fault structures, and their influence on earthquake source processes,
95 as demonstrated in other regional studies (Bokelmann & Beroza, 2000; Li et al., 2018).
96 In this study we take advantage of a new catalog of 161 FMS ($M 1.5+$) calculated using a full-
97 waveform moment tensor inversion technique to investigate the spatial variations in stress field
98 orientation with respect to the earthquake distribution in the CSZ. We combine FMS with
99 existing data to determine the orientation and relative magnitudes of the principal stresses with
100 particular focus on depth-dependent variations. We show the maximum horizontal stress rotates
101 clockwise with depth from the near surface approximately river-parallel borehole breakout
102 orientation toward roughly river-perpendicular maximum strain rate direction inferred in the
103 lower crust. The stress rotation occurs primarily in the middle crust (~ 13 - 26 km), where the
104 effect of postglacial rebound is amplified by a “weaker” crust with low frictional strength and
105 semi-brittle rheology.

106

107 **2. Data and Methods**

108 We use a dataset of 1760 earthquakes ($M_N -0.7 - 5.4$; M_N is Nuttli magnitude (Nuttli, 1973)) that
109 occurred in the CSZ between January 1988 and August 2017 (Figure 1a), with a ~ 2 years gap
110 between 2010 and 2012 built from combining the relocated earthquake catalogs of Yu et al.
111 (2016a) and Onwuemeka et al. (2018). We calculate the b -value and the magnitude of
112 completeness (M_c) of the relocated catalog using the maximum likelihood method (Utsu, 1965)
113 and Goodness-of-Fit test (Wiemer & Wyss, 2000), respectively, using the mean values of 1000
114 bootstrap runs and the 68% confidence intervals.

115 We apply the probabilistic earthquake source inversion framework *Grond* (Heimann et
116 al., 2018) to perform full moment tensor inversion of 161 M 1.3+ events reported between April
117 2000 and February 2018. We use waveform data recorded by seven CNSN stations (CN network,
118 operational since October 1994), six Quebec-Maine Transect campaign stations (X8 network,
119 August 2012-August 2016), two USArray Transportable Array campaign stations (TA network,
120 August 2013-July 2015;), and four temporary McGill University stations (MG network, since
121 July 2015) in the Charlevoix area. Following Onwuemeka et al. (2018), we use the St. Lawrence
122 River south shore velocity model of Lamontagne (1999) to precalculate Green's Functions (GF)
123 for modeling synthetic seismograms. Text S1 details the moment tensor inversion. We augment
124 our solutions with 64 additional FMS (63 FMS of events occurring between June 1974 and
125 October 1997 and 1 FMS of the 1925 M 6.2 Charlevoix – Kamouraska event) of varying quality
126 factors (27 A, 11 B, 24 C, and 2 D; quality factor decreases alphabetically) computed by
127 Mazzotti & Townend (2010). We then use the combined 225 FM (Figure 1b) to invert for the
128 principal stress orientations, stress ratio $R = (\sigma_1 - \sigma_2) / (\sigma_1 - \sigma_3)$, and apparent friction coefficient
129 (μ) through an iterative joint focal mechanism inversion (STRESSINVERSE, Vavryčuk, 2014).
130 Following Abolfathian et al. (2019) we refer to μ as the apparent friction coefficient, which is
131 calculated in the stress inversion procedure. A bootstrap resampling (500) of the original set of
132 225 FMS constrains the 95% confidence intervals. In addition, we determine the orientation of
133 the maximum horizontal stress, S_{Hmax} , with the method of Lund & Townend (2007). Text S2
134 details the standard stress inversion procedure.

135

136

137

138 3. Results

139 3.1 Spatial variability of b -value in the CSZ

140 The estimated M_c and b -value for the entire catalog are 1.86 and 0.96 (0.92 – 0.99), respectively
141 (Figure S1a). The 1432 events located within the impact structure have calculated M_c of 1.92 and
142 b -values of 1.06 (1.02 – 1.09), while M_c and b -values of the 328 events located outside the
143 impact structure are 1.54 and 0.70 (0.67 – 0.72), respectively (Figure S1b, c). To avoid bias in b -
144 value estimation due to changes in M_c (Hainzl, 2016), we also calculate b -values using a fixed
145 M_c equal to the one estimated for the entire catalog (1.86). The resulting values of 1.05 (1.03 –
146 1.07) for the events within the impact crater, and 0.78 (0.75 – 0.81) for events outside are in
147 agreement with results from Yu et al., (2016a).

148 Furthermore, we compute the depth-dependent variation of M_c and b -value using 50%
149 overlapping windows of 300 events (Figure 2). Depth-dependent changes in b -value and M_c
150 appear to follow a similar trend (Figure 2b, c). In order to increase the estimate robustness, we
151 recalculate b -values at a fixed M_c (1.86) for each depth interval (Figure 2d). Figure 2d shows
152 results from both the entire catalog (black points and line), and events within the impact structure
153 (magenta points and line). The b -values of the entire catalog clearly decrease with depth from ~
154 1.1 to ~ 0.9 until approximately 12 km, followed by a brief rebound to ~ 1.0 for about 1 km,
155 before returning to ~ 0.9 at greater depth. Events within the impact structure show b -values
156 similar to the entire catalog until ~10 km depth, followed by a sudden increase with depth that
157 peaks at ~1.2 at ~ 12.5 km. Between ~12.5 km and 15 km, b -values are similar between the two
158 groups. Below ~15 km, the events within the impact zone exhibit higher b -values relative to the
159 full catalog, although the estimates are less well-constrained due to the decrease of seismicity
160 with depth (Figure 2a). The strong contrast in the b -value-depth variation between the two event

161 populations likely results from the fact that seven of eight $M_N \geq 4$ earthquakes in the full catalog
162 occurred outside the impact structure (Figure 2d), causing a strong statistical bias toward the
163 larger magnitude events in the b -value estimate.

164

165 **3.2 Focal mechanisms and moment tensor inversion**

166 The majority of the earthquakes exhibit reverse-faulting kinematics (Figure 1b) consistent with
167 reverse-sense reactivation of pre-existing Iapetus normal faults (e.g., Mazzotti & Townend,
168 2010; Onwuemeka et al., 2018). The extensive damage and relative higher fault/fracture density
169 produced by the meteorite impact likely explain the higher diversity of FMS within the impact
170 structure relative to other locations in the CSZ (Yu et al., 2016a).

171 Stress inversion results of the 225 FMs produce a maximum principal stress (σ_1) with a mean
172 azimuth of 93° (Figure 1b), a roughly vertical minimum principal stress (σ_3), and intermediate
173 principle stress (σ_2) with a mean azimuth of 184° . The estimated S_{Hmax} has a mean azimuth of
174 90.7° , which represents a clockwise rotation from the regional S_{Hmax} of 54° determined from
175 borehole breakout studies (Mazzotti & Townend, 2010). Stress ratios R range between 0.26 and
176 0.56 with mean value of 0.41.

177 We evaluate the stress variation with depth by inverting for the principle-stress
178 orientations in subset groups of 75 events overlapping by 60 events. We also invert for the
179 maximum horizontal stress (S_{Hmax}), the stress ratio (R), and apparent friction coefficient (μ)
180 within subsets (Figure 3). The results show a depth-dependent clockwise rotation of both σ_1 and
181 σ_2 (Figure 3a, b). Mean values of σ_1 and σ_2 remain constant down to ~ 12.5 km within the 95%
182 confidence intervals, with the largest stress rotation of σ_1 from azimuth $\sim 80^\circ$ to 110° and σ_2 from
183 $\sim 170^\circ$ to 200° between ~ 12.5 and ~ 16 km depth. The inversion results show no additional stress

184 rotation below ~16 km. In addition to the azimuth rotation of σ_1 and σ_2 , the σ_1 plunge rotates
185 from near-horizontal ($\sim 5^\circ$) to a shallow dip angle ($\sim 15^\circ$) at ~15 km depth (Figure 3c). Our
186 results also show a decreasing trend with depth of both the R value from 0.7 at shallow depths to
187 0.25 at ~16 km and μ from 0.8 to 0.45 over the same depth range (Figure 3d, e). Finally, the
188 results show a total clockwise rotation of S_{Hmax} of $\sim 30^\circ$ (82.5° to 111.8°) between shallow and
189 deeper FMS (consistent with the σ_1 and σ_2 azimuthal rotations) and a total clockwise rotation of
190 $\sim 58^\circ$ from the regional S_{Hmax} of 54° determined from borehole breakouts (Mazzotti & Townend,
191 2010) (Figure 3f).

192

193 **4. Discussion**

194 The S_{Hmax} orientation from borehole breakouts in eastern Canada suggests that a roughly NE –
195 SW compression drives stress perturbation. Under a NE – SW compressive stress regime,
196 Iapetan faults in the CSZ are not optimally-oriented for thrust faulting, and therefore require an
197 additional perturbation of stress orientation to explain the prevalent thrust and reverse – oblique
198 kinematics presently observed. “Weak” faults are a plausible cause for reactivation of non-
199 optimally-oriented faults. Explanations for fault weakening include weak fault materials (clay-
200 rich gouge) (Ikari et al., 2009), dynamic slip weakening and shear heating (Di Toro et al., 2006;
201 Wibberley & Shimamoto, 2005), damage-induced changes in elastic properties (high fracture
202 density) (Faulkner et al., 2006), and elevated pore fluid pressure (Byerlee, 1990).

203 Previous studies in eastern North America have proposed that postglacial isostatic rebound
204 stresses following the Wisconsin glaciation (85 - 11 kyr) concentrate on faults by localized
205 weaknesses (e.g., dense fracture networks) (e.g., Mazzotti & Townend, 2010; Wu & Hasegawa,
206 1996). Such stress concentrations on pre-existing zones of weakness may be the most probable

207 source of stress perturbation and driving mechanism of the observed stress rotation. Although the
208 magnitude of post-glacial isostatic rebound stresses are on the order of kPa, localized weaknesses
209 within the highly fractured Charlevoix impact structure may locally enhance stresses. Tarayoun
210 et al. (2018) found that localized structural inheritance amplifies surface strain across St.
211 Lawrence Valley, suggesting that post-glacial isostatic rebound stresses causes significant stress
212 perturbations in structurally weak zones.

213

214 The stress orientation observed here (Figure 1b) agrees with previous work. For example,
215 Mazzotti & Townend (2010) found that S_{Hmax} is rotated by up to 47° (when considering the
216 south-eastern cluster) in the CSZ with respect to the borehole breakout measurements. We note
217 that the 64 of the FMS common to this study and Mazzotti & Townend (2010) make up less than
218 30 % of our dataset, and would unlikely bias our results. Similar clockwise S_{Hmax} rotations of 44°
219 and 49° are reported for the Lower Saint Lawrence Seismic Zone (SLZ) north of the CSZ,
220 respectively, by Mazzotti & Townend (2010) and Plourde & Nedimović (2021). Furthermore,
221 Plourde & Nedimović (2021) also observed a clockwise rotation of $\sim 49^\circ$ of σ_I with depth in the
222 LSZ, mostly inferred from mid-crustal depths. Similarly, our results show the largest clockwise
223 rotation below ~ 13 km (Figures 3, and 4), which roughly represents the transition from upper to
224 middle crust in the CSZ (Laske et al., 2013). The pronounced stress rotation observed in both the
225 LSZ and CSZ are consistent with a “weaker” middle crust in both seismic zones. Mazzotti &
226 Townend (2010) also observed that the largest S_{Hmax} rotation inferred from the cluster of events
227 located southeast of the Saint-Laurent fault (Figure S2) relative to the cluster to the northwest.
228 The difference can be explained by the depth-dependent rotation observed in this study, namely,
229 the larger number of shallow events in the northern cluster (0 – 7 km) (Figure S2) results in a

230 smaller stress rotation, whereas the relatively deeper southern cluster reflects the deeper, hence
231 larger stress rotation.

232 The apparent friction coefficient (μ) calculated by the stress inversion also supports the “weaker”
233 middle crust hypothesis, with highest values of μ (0.65 – 0.8) in the upper crust and lower
234 relative values in the middle crust (0.45 – 0.6) (Figure 3e). A decrease in μ with depth would also
235 explain the decrease in R (Figure 3d). The differential stress ($\sigma_1 - \sigma_3$) for thrust faulting can be
236 expressed as follows (Sibson, 1974):

$$237 \quad (\sigma_1 - \sigma_3) = (F-1) \rho g z (1-\lambda)$$

238 where $F = [(1+\mu^2)^{1/2} + \mu]^2$, ρ is the average crustal density, g is the gravitational acceleration, z
239 is the depth, and $\lambda = P_f/\rho g z$ is the pore fluid factor, with P_f being pore fluid pressure. For thrust
240 faulting $\sigma_3 = (1-\lambda) \rho g z$ (vertical stress), and $\sigma_1 = F\sigma_3$ (maximum horizontal stress), making σ_1
241 dependent on the friction coefficient (μ). Therefore, a decrease in μ will result in a decrease of
242 both $\sigma_1 - \sigma_2$ and $\sigma_1 - \sigma_3$, and a subsequent decrease in R . However, the previous statement is only
243 valid if both σ_2 and σ_3 are not affected by the change of μ .

244
245 Similar to the stress inversion results, depth-dependent b -values also show a significant change at
246 the upper – middle crust boundary (12 km - 13 km) (Figure 2d). The b -values clearly decrease
247 with depth until ~12 km and start increasing again following a variable trend. We evaluate
248 possible effects of using M_N in our calculations, and convert M_N to M_W following Bent (2011).
249 Figure S3 shows the M_W depth-dependent b -values follow a similar trend to M_N values (Figure
250 2). The inverse depth and b -value relationship observed in the upper crust of the CSZ is
251 consistent with of Amitrano (2003) and Spada et al., (2013), both of whom observed decreasing
252 b -values with increasing confining pressure and differential stress. Spada et al. (2013) also

253 suggested that the change in the monotonic trend of b -value may reflect the location of the
254 brittle-ductile transition. However, the observed trend reversal in b -value at ~ 12.5 km (Figure 2)
255 may not reflect the brittle-ductile transition where seismicity typically diminishes with depth.
256 Rather, seismicity here peaks around 12.5 km and remains abundant down to ~ 22 km (Figure
257 2a). Therefore, we hypothesize that upper – middle crust boundary located at ~ 12.5 km may
258 instead represent a transition from a brittle behavior of the upper crust to a semi-brittle behavior
259 of the middle crust, where brittle and ductile mechanisms coexist or alternate. The transition to a
260 fully ductile regime likely occurs at ~ 26 km depth at the limit between middle and lower crust
261 (Figure 4).

262

263 The discussion in the preceding paragraph accounts for all the events in the catalog. The
264 significantly higher b -values between 10 km and 13 km within the impact structure support the
265 presence of a locally highly fractured and weak upper crust (Yu et al., 2016a). The higher local
266 b -values are particularly important for probabilistic seismic hazard assessment, given the
267 implications on the frequency of possible future large earthquakes implied by b -values. Our
268 results suggest a relatively higher seismic hazard outside the impact structure, when solely based
269 on b -values. However, Yu et al. (2016a) interpreted the seismic moment deficit within the impact
270 structure could imply a higher seismic hazard, if the moment deficit is the manifestation of
271 locked faults storing accumulated strain energy. The authors also suggested that aseismic creep
272 and strain release might hinder significant strain energy accumulation. However, the overall low
273 geodetic strain rates in this area (Mazzotti & Adams, 2005; Sella et al., 2007) make it
274 challenging to evaluate which of the above two scenarios is more plausible.

275

276 Figure 4 provides a conceptual framework of the crustal rheological structure in the CSZ
277 interpreted from the results of this work. The mostly reverse faulting kinematics inferred from
278 FM solutions in the CSZ (Figure 1b) are consistent with the horizontal compressional stress
279 induced by the postglacial unloading following the Wisconsin glaciation (85 – 11 kyr) (Figure
280 4b) that is likely amplified by pre-existing structural weakness. The stress inversion results, in
281 particular the depth-variable maximum horizontal stress S_{Hmax} , clearly depict systematic
282 clockwise rotation from the NE-SW orientation inferred from shallow borehole measurements (~
283 parallel to the St Lawrence River) toward a NW-SE orientation (~ perpendicular to the SLR).
284 The rotated NW-SE S_{Hmax} direction is consistent with maximum strain predicted by Glacial
285 Isostatic Adjustment (GIA) models (Peltier et al., 2015). The largest S_{Hmax} rotation of up to ~ 60°
286 from borehole breakouts is reached at mid-crustal depths ~ 20-26 km, where seismicity ceases.
287 No earthquake FMS are available for stress inversion at greater depth, however, it is plausible
288 that the clockwise rotation continues to approach the GIA estimated strain direction (Figure 4c).
289 The large rotation is possibly due to a significant change in rheological and frictional properties
290 of the middle crust as suggested by the depth-dependent b -value and μ variations (Figure 4d).
291 Based on the above interpretations, we hypothesize a rheological profile including a brittle upper
292 crust, a semi-brittle middle crust, and a ductile lower crust (Figure 4d). Finally, the rotation of
293 the σ_1 plunge from near-horizontal (~5°) at the upper crust to shallowly dipping (~15°) at middle
294 crust may reflect the initiation of the gradual transition with depth from a compressional (σ_1
295 horizontal) to an extensional regime (σ_1 vertical), as is expected under the influence of
296 postglacial rebound (Figure 4a, 4b). Similar to the S_{Hmax} rotation, our stress inversion results can
297 only capture the initial phase of σ_1 plunge rotation (due to the depth limits of seismicity) that
298 likely continues with depth.

299

300 Several studies have shown that large earthquakes may produce temporal principal stress
301 rotations in different tectonic settings (Hardebeck & Okada, 2018; Yu et al., 2016b). Here, we
302 use the software Coulomb 3.4 (Toda et al., 2011) to test the extent to which the 1663 M 6+
303 (Ebel, 2011) event influences the regional stress orientation (Text S3 for details). Our results
304 (Figure S4) show that significant stress rotation occurs within the context of low background
305 differential stress. However, independent of the differential stress, none of the modeled cases
306 explored here accurately represent the present state of stress in the CSZ (Figure 1b). In addition,
307 regional stresses are expected to return to their pre-mainshock orientation within a few months to
308 years (Hardebeck, 2012; Hardebeck & Okada, 2018). Therefore, stress enhancement due to
309 localized weakness, post-glacial isostatic rebound, and ridge-push forces, must be invoked to
310 adequately quantify higher seismic hazard in intraplate seismic zones (e.g., CSZ) in eastern
311 North America.

312

313 **5. Conclusions**

314 We combine a methodology based on the stress inversion of 225 FMS with the frequency-
315 magnitude distribution properties of earthquakes to investigate the spatial variation of stress field
316 and crustal strength in the CSZ. Our results show that:

- 317 • The $\sim 40^\circ$ clockwise rotations of S_{Hmax} obtained from the inversion of the entire FMS
318 catalog supports the hypothesis that pre-existing weaknesses in the CSZ amplify
319 postglacial horizontal stresses.

- 320 • The large S_{Hmax} rotation below ~ 13 km depth is consistent with variable rheological and
321 frictional properties of the middle crust, suggesting low friction coefficient and semi-
322 brittle behavior, which further amplify postglacial rebound stresses.
- 323 • The monotonic decrease of b -value with depth in the upper ~ 13 km suggest an inverse
324 relationship with differential stress in the upper crust. The relationship becomes
325 insignificant in the middle crust due to its differing rheology.
- 326 • Historical large earthquakes do not significantly affect the present-day stress state in the
327 CSZ.

328

329 **Acknowledgements**

330 We thank Pierre Archambault, Maurice Lamontagne, and Alain Tremblay for their assistance in
331 the deployment and maintenance of the McGill stations in Charlevoix. This work is supported by
332 the Team Research Program of the Fonds de Recherche du Québec - Nature et Technologies
333 (PR-191259), and the Natural Sciences and Engineering Research Council of Canada (NSERC)
334 Discovery Grant (RGPIN-2018-05389).

335

336

337 **Open Research**

338 The relocated catalog and the focal mechanisms solutions from this work are available in the
339 Zenodo data repository (<https://doi.org/10.5281/zenodo.6786234>).

340

341

342

343 **References**

- 344 Abolfathian, N., Martínez-Garzón, P., & Ben-Zion, Y. (2019). Spatiotemporal Variations of Stress and
345 Strain Parameters in the San Jacinto Fault Zone. *Pure and Applied Geophysics*, 176(3), 1145–1168.
346 <https://doi.org/10.1007/s00024-018-2055-y>
- 347 Adams, J., & Basham, P. (1991). The seismicity and seismotectonics of eastern Canada.
348 <https://doi.org/10.1130/DNAG-CSMS-NEO.261>
- 349 Amitrano, D. (2003). Brittle-ductile transition and associated seismicity: Experimental and numerical
350 studies and relationship with the b value. *Journal of Geophysical Research: Solid Earth*, 108(B1).
351 <https://doi.org/10.1029/2001JB000680>
- 352 Bent, A. L. (2011). Moment Magnitude (Mw) Conversion Relations for Use in Hazard Assessment in
353 Eastern Canada. *Seismological Research Letters*, 82(6), 984–990. <https://doi.org/10.1785/gssrl.82.6.984>
- 354 Bokelmann, G. H. R., & Beroza, G. C. (2000). Depth-dependent earthquake focal mechanism orientation:
355 Evidence for a weak zone in the lower crust. *Journal of Geophysical Research: Solid Earth*, 105(B9),
356 21683–21695. <https://doi.org/10.1029/2000JB900205>
- 357 Byerlee, J. (1990). Friction, overpressure and fault normal compression. *Geophysical Research Letters*,
358 17(12), 2109–2112. <https://doi.org/10.1029/GL017i012p02109>
- 359 Di Toro, G., Hirose, T., Nielsen, S., Pennacchioni, G., & Shimamoto, T. (2006). Natural and Experimental
360 Evidence of Melt Lubrication of Faults During Earthquakes. *Science*, 311(5761), 647–649.
361 <https://doi.org/10.1126/science.1121012>
- 362 Ebel, J. E. (2011). A New Analysis of the Magnitude of the February 1663 Earthquake at Charlevoix,
363 Quebec
364 *Bulletin of the Seismological Society of America*, 101(3), 1024–1038.
365 <https://doi.org/10.1785/0120100190>
- 366 Faulkner, D. R., Mitchell, T. M., Healy, D., & Heap, M. J. (2006). Slip on “weak” faults by the rotation of
367 regional stress in the fracture damage zone. *Nature*, 444(7121), 922–925.
368 <https://doi.org/10.1038/nature05353>
- 369 Hainzl, S. (2016). Rate-Dependent Incompleteness of Earthquake Catalogs. *Seismological Research*
370 *Letters*, 87(2A), 337–344. <https://doi.org/10.1785/0220150211>
- 371 Hardebeck, J. L., & Hauksson, E. (2001). Crustal stress field in southern California and its implications for
372 fault mechanics. *Journal of Geophysical Research: Solid Earth*, 106(B10), 21859–21882.
373 <https://doi.org/10.1029/2001JB000292>
- 374 Hardebeck, J. L., & Okada, T. (2018). Temporal Stress Changes Caused by Earthquakes: A Review. *Journal*
375 *of Geophysical Research: Solid Earth*, 123(2), 1350–1365. <https://doi.org/10.1002/2017JB014617>
- 376 Heimann, S., Isken, M., Kühn, D., Sudhaus, H., Steinberg, A., Daout, S., et al. (2018). Grond - A
377 probabilistic earthquake source inversion framework (Version 1.0) [Application/octet-
378 stream,application/octet-stream,application/octet-stream,application/octet-stream,application/octet-
379 stream]. GFZ Data Services. <https://doi.org/10.5880/GFZ.2.1.2018.003>

380 Ikari, M. J., Saffer, D. M., & Marone, C. (2009). Frictional and hydrologic properties of clay-rich fault
381 gouge. *Journal of Geophysical Research: Solid Earth*, 114(B5). <https://doi.org/10.1029/2008JB006089>

382 Johnston, A. C. (1989). The Seismicity of 'Stable Continental Interiors.' In S. Gregersen & P. W. Basham
383 (Eds.), *Earthquakes at North-Atlantic Passive Margins: Neotectonics and Postglacial Rebound* (pp. 299–
384 327). Dordrecht: Springer Netherlands. https://doi.org/10.1007/978-94-009-2311-9_18

385 Lamontagne, M. (1987). Seismic activity and structural features in the Charlevoix region, Quebec.
386 *Canadian Journal of Earth Sciences*, 24(11), 2118–2129. <https://doi.org/10.1139/e87-202>

387 Lamontagne, M. (1999, January 1). *Rheological and geological constraints on the earthquake distribution*
388 *in the Charlevoix Seismic Zone, Quebec, Canada. Ph.D. Thesis*. Retrieved from
389 <https://ui.adsabs.harvard.edu/abs/1999PhDT>

390 Lemieux, Y., Tremblay, A., & Lavoie, D. (2003). Structural analysis of supracrustal faults in the Charlevoix
391 area, Quebec: relation to impact cratering and the St-Laurent fault system. *Canadian Journal of Earth*
392 *Sciences*, 40(2), 221–235. <https://doi.org/10.1139/e02-046>

393 Li, D., McGuire, J. J., Liu, Y., & Hardebeck, J. L. (2018). Stress rotation across the Cascadia megathrust
394 requires a weak subduction plate boundary at seismogenic depths. *Earth and Planetary Science Letters*,
395 485, 55–64. <https://doi.org/10.1016/j.epsl.2018.01.002>

396 Lund, B., & Townend, J. (2007). Calculating horizontal stress orientations with full or partial knowledge
397 of the tectonic stress tensor. *Geophysical Journal International*, 170(3), 1328–1335.
398 <https://doi.org/10.1111/j.1365-246X.2007.03468.x>

399 Mazzotti, S., & Adams, J. (2005). Rates and uncertainties on seismic moment and deformation in eastern
400 Canada. *Journal of Geophysical Research: Solid Earth*, 110(B9). <https://doi.org/10.1029/2004JB003510>

401 Mazzotti, S., & Gueydan, F. (2018). Control of tectonic inheritance on continental intraplate strain rate
402 and seismicity. *Tectonophysics*, 746, 602–610. <https://doi.org/10.1016/j.tecto.2017.12.014>

403 Mazzotti, S., & Townend, J. (2010). State of stress in central and eastern North American seismic zones.
404 *Lithosphere*, 2(2), 76–83. <https://doi.org/10.1130/L65.1>

405 Mori, J., & Abercrombie, R. E. (1997). Depth dependence of earthquake frequency-magnitude
406 distributions in California: Implications for rupture initiation. *Journal of Geophysical Research: Solid*
407 *Earth*, 102(B7), 15081–15090. <https://doi.org/10.1029/97JB01356>

408 Nuttli, O. W. (1973). Seismic wave attenuation and magnitude relations for eastern North America.
409 *Journal of Geophysical Research (1896-1977)*, 78(5), 876–885.
410 <https://doi.org/10.1029/JB078i005p00876>

411 Onwuemeka, J., Liu, Y., & Harrington, R. M. (2021). Crustal Velocity Variations and Constraints on
412 Material Properties in the Charlevoix Seismic Zone, Eastern Canada. *Journal of Geophysical Research:*
413 *Solid Earth*, 126(7), e2020JB020918. <https://doi.org/10.1029/2020JB020918>

414 Onwuemeka, J., Liu, Y., & Harrington, R. M. (2018). Earthquake Stress Drop in the Charlevoix Seismic
415 Zone, Eastern Canada. *Geophysical Research Letters*, 45(22), 12,226–12,235.
416 <https://doi.org/10.1029/2018GL079382>

417 Peltier, W. R., Argus, D. F., & Drummond, R. (2015). Space geodesy constrains ice age terminal
418 deglaciation: The global ICE-6G_C (VM5a) model. *Journal of Geophysical Research: Solid Earth*, *120*(1),
419 450–487. <https://doi.org/10.1002/2014JB011176>

420 Plourde, A. P., & Nedimović, M. R. (2021). Earthquake Depths, Focal Mechanisms, and Stress in the
421 Lower St. Lawrence Seismic Zone. *Seismological Research Letters*, *92*(4), 2562–2572.
422 <https://doi.org/10.1785/0220200429>

423 Quinlan, G. (1984). Postglacial rebound and the focal mechanisms of eastern Canadian earthquakes.
424 *Canadian Journal of Earth Sciences*, *21*(9), 1018–1023. <https://doi.org/10.1139/e84-106>

425 Rondot, J. (1971). Impactite of the Charlevoix Structure, Quebec, Canada. *Journal of Geophysical*
426 *Research*, *76*(23), 5414–5423. <https://doi.org/10.1029/JB076i023p05414>

427 Schmieder, M., Shaulis, B. J., Lapen, T. J., Buchner, E., & Kring, D. A. (2019). In situ U–Pb analysis of
428 shocked zircon from the Charlevoix impact structure, Québec, Canada. *Meteoritics & Planetary Science*,
429 *54*(8), 1808–1827. <https://doi.org/10.1111/maps.13315>

430 Sella, G. F., Stein, S., Dixon, T. H., Craymer, M., James, T. S., Mazzotti, S., & Dokka, R. K. (2007).
431 Observation of glacial isostatic adjustment in “stable” North America with GPS. *Geophysical Research*
432 *Letters*, *34*(2). <https://doi.org/10.1029/2006GL027081>

433 Sibson, R. H. (1974). Frictional constraints on thrust, wrench and normal faults. *Nature*, *249*(5457), 542–
434 544. <https://doi.org/10.1038/249542a0>

435 Spada, M., Tormann, T., Wiemer, S., & Enescu, B. (2013). Generic dependence of the frequency-size
436 distribution of earthquakes on depth and its relation to the strength profile of the crust. *Geophysical*
437 *Research Letters*, *40*(4), 709–714. <https://doi.org/10.1029/2012GL054198>

438 Stein, S., & Mazzotti, S. (2007). Continental Intraplate Earthquakes: Science, Hazard, and Policy Issues.
439 <https://doi.org/10.1130/SPE425>

440 van Stiphout, T., Kissling, E., Wiemer, S., & Ruppert, N. (2009). Magmatic processes in the Alaska
441 subduction zone by combined 3-D b value imaging and targeted seismic tomography. *Journal of*
442 *Geophysical Research: Solid Earth*, *114*(B11). <https://doi.org/10.1029/2008JB005958>

443 Tarayoun, A., Mazzotti, S., Craymer, M., & Henton, J. (2018). Structural Inheritance Control on Intraplate
444 Present-Day Deformation: GPS Strain Rate Variations in the Saint Lawrence Valley, Eastern Canada.
445 *Journal of Geophysical Research: Solid Earth*, *123*(8), 7004–7020. <https://doi.org/10.1029/2017JB015417>

446 Toda, S., Stein, R. S., Sevilgen, V., & Lin, J. (2011). *Coulomb 3.3 Graphic-rich deformation and stress-*
447 *change software for earthquake, tectonic, and volcano research and teaching-user guide* (USGS
448 Numbered Series No. 2011–1060). *Coulomb 3.3 Graphic-rich deformation and stress-change software*
449 *for earthquake, tectonic, and volcano research and teaching-user guide* (Vol. 2011–1060). Reston, VA:
450 U.S. Geological Survey. <https://doi.org/10.3133/ofr20111060>

451 Utsu, T. (1965). A method for determining the value of. *Geophys. Bull. Hokkaido Univ.*, *13*, 99–103.

452 Vavryčuk, V. (2014). Iterative joint inversion for stress and fault orientations from focal mechanisms.
453 *Geophysical Journal International*, *199*(1), 69–77. <https://doi.org/10.1093/gji/ggu224>

454 Wibberley, C. A. J., & Shimamoto, T. (2005). Earthquake slip weakening and asperities explained by
455 thermal pressurization. *Nature*, 436(7051), 689–692. <https://doi.org/10.1038/nature03901>

456 Wiemer, S., & Wyss, M. (2000). Minimum Magnitude of Completeness in Earthquake Catalogs: Examples
457 from Alaska, the Western United States, and Japan. *Bulletin of the Seismological Society of America*,
458 90(4), 859–869. <https://doi.org/10.1785/0119990114>

459 Wu, P., & Hasegawa, H. S. (1996). Induced stresses and fault potential in eastern Canada due to a
460 realistic load: a preliminary analysis. *Geophysical Journal International*, 127(1), 215–229.
461 <https://doi.org/10.1111/j.1365-246X.1996.tb01546.x>

462 Yu, H., Liu, Y., Harrington, R. M., & Lamontagne, M. (2016). Seismicity along St. Lawrence Paleorift Faults
463 Overprinted by a Meteorite Impact Structure in Charlevoix, Québec, Eastern Canada. *Bulletin of the*
464 *Seismological Society of America*, 106(6), 2663–2673. <https://doi.org/10.1785/0120160036>

465 Yu, H., Zhao, L., Liu, Y., Ning, J., Chen, Q.-F., & Lin, J. (2016). Stress adjustment revealed by seismicity and
466 earthquake focal mechanisms in northeast China before and after the 2011 Tohoku-Oki earthquake.
467 *Tectonophysics*, 666, 23–32. <https://doi.org/10.1016/j.tecto.2015.10.009>

468

469 **Figure captions**

470 **Figure 1.** Seismicity in the Charlevoix Seismic Zone (CSZ). (a) Map of relocated earthquakes
471 that occurred between January 1988 and August 2017. Events are color-coded by hypocentral
472 depth. (b) Focal mechanism solutions (FMS) used in this study with the lower-right inset
473 showing the results of the stress inversion from all the FMS. Solid black lines indicate known
474 faults (Lamontagne, 1999; Rondot, 1971). Dashed circles indicate inner and outer boundaries of
475 the meteorite impact structure. Black arrows indicate orientation of maximum horizontal stress
476 from borehole breakouts.

477

478 **Figure 2.** Magnitude-frequency distribution of relocated earthquakes in the CSZ. (a) Distribution
479 of earthquakes with depth. (b) Depth-dependent variation of magnitude of completeness (M_c)
480 calculated using moving windows of 300 events with 150-event overlap. (c) Depth-dependent b -
481 value calculated using M_c in (b). (d) Depth-dependent b -value variation of using a fixed $M_c =$
482 1.86. Black points represent b -values for the entire catalog, magenta points indicate b -values for

483 events within the impact structure. Grey bars indicate distribution of $M_N \geq 4$ events in the entire
484 catalog (light) and within the events located inside the impact structure.

485

486 **Figure 3.** Depth-dependent variation of (a) σ_1 azimuth, (b) σ_2 azimuth, (c) σ_1 and σ_2 plunge, (d)
487 stress ratio, and (e) apparent friction coefficient in moving windows of 75 events, overlapping by
488 15 events. Vertical lines represent depth range of the FMS used in each window, horizontal lines
489 indicate 95% confidence interval. (f) Polar plots of specific stress inversions denoted by numbers
490 (1-3). Black solid lines represent the orientation of the maximum horizontal stress (S_{Hmax}), with
491 black dashed lines indicating 95% confidence interval limits of the. Grey solid lines represent the
492 S_{Hmax} orientation from borehole breakouts (Mazzotti & Townend, 2010).

493

494 **Figure 4.** Schematic NW-SE cross section showing the expected horizontal stress distribution in
495 the lithosphere during (a) glacial loading and (b) postglacial unloading following Wisconsin
496 glaciation (85-11 kyr). (c) Conceptual model showing crustal depth-dependent clockwise
497 rotation of maximum horizontal stress (S_{Hmax}) in the CSZ calculated here (black arrows)
498 compared to S_{Hmax} from borehole breakouts data (grey arrows), and maximum horizontal strain
499 direction from GIA modeling (Peltier et al., 2015). (d) Hypothetical rheological profile of the
500 crust (solid lines color-coded by section of the crust) in the CSZ based on the distribution of
501 earthquakes (grey histogram), b -value (dashed red line), apparent friction coefficient (μ) (dashed
502 black line). Black arrows show the calculated rotation of the σ_1 plunge interpreted as possible
503 transition to an extensional regime approaching the neutral plane (a, b). Vertical and horizontal
504 axis do not have the same scale.

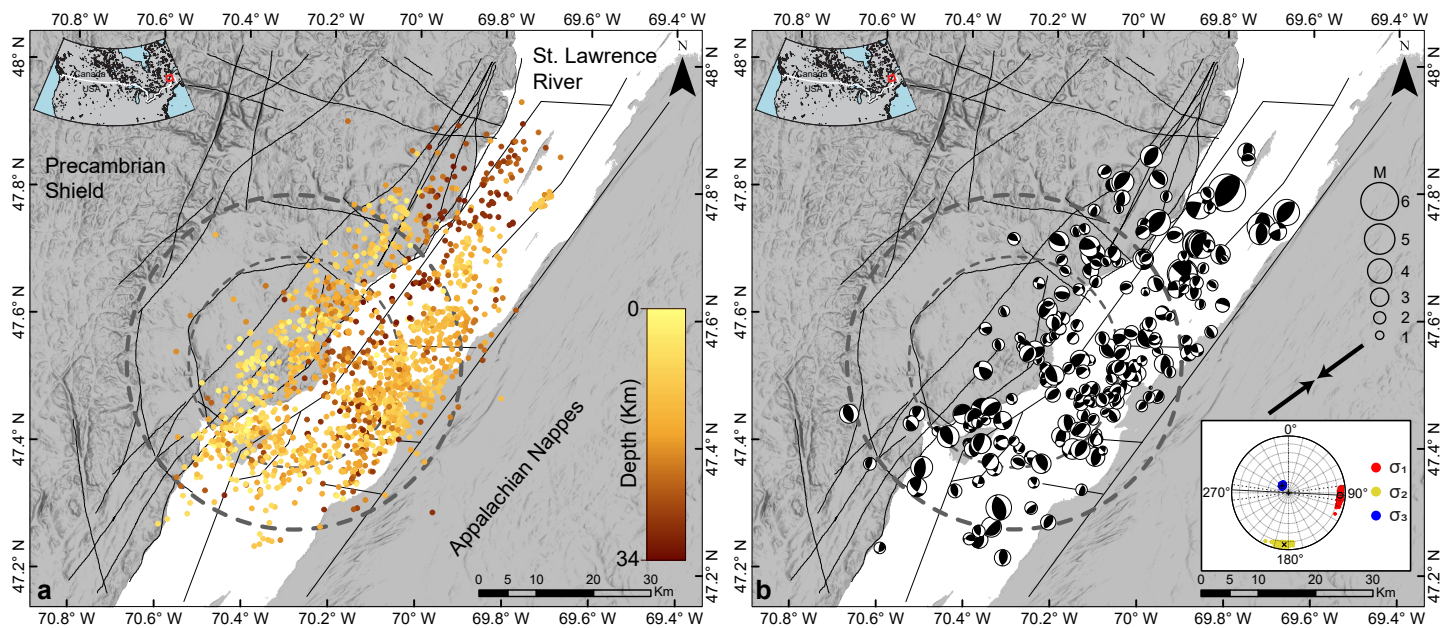


Figure 1. Seismicity in the Charlevoix Seismic Zone (CSZ). (a) Map of relocated earthquakes that occurred between January 1988 and August 2017. Events are color-coded by hypocentral depth. (b) Focal mechanism solutions (FMS) used in this study with the lower-right inset showing the results of the stress inversion from all the FMS. Solid black lines indicate known faults (Lamontagne, 1999; Rondot, 1971). Dashed circles indicate inner and outer boundaries of the meteorite impact structure. Black arrows indicate orientation of maximum horizontal stress from borehole break-outs.

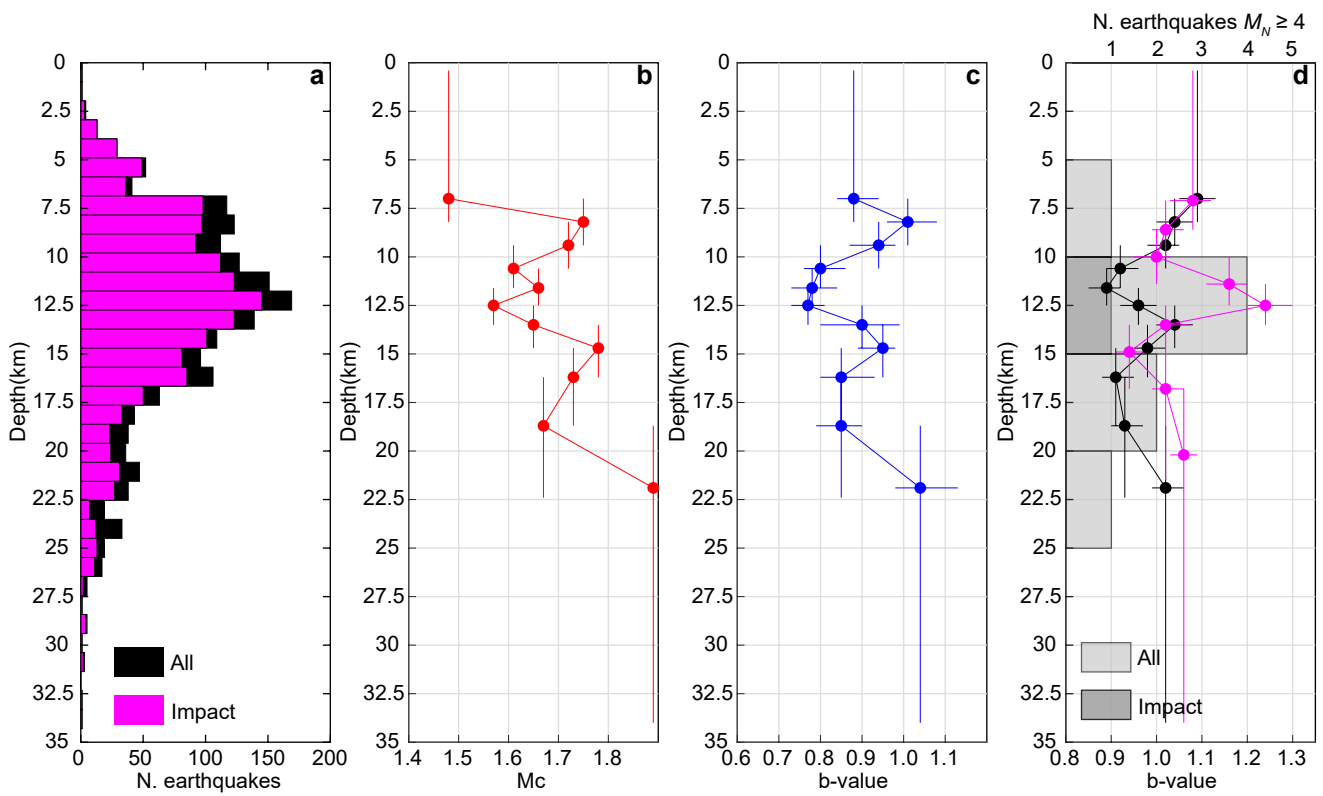


Figure 2. Magnitude-frequency distribution of relocated earthquakes in the CSZ. (a) Distribution of earthquakes with depth. (b) Depth-dependent variation of magnitude of completeness (M_c) calculated using moving windows of 300 events with 150-event overlap. (c) Depth-dependent b-value calculated using M_c in (b). (d) Depth-dependent b-value variation of using a fixed $M_c = 1.86$. Black points represent b-values for the entire catalog, magenta points indicate b-values for events within the impact structure. Grey bars indicate distribution of $M_N \geq 4$ events in the entire catalog (light) and within the events located inside the impact structure.

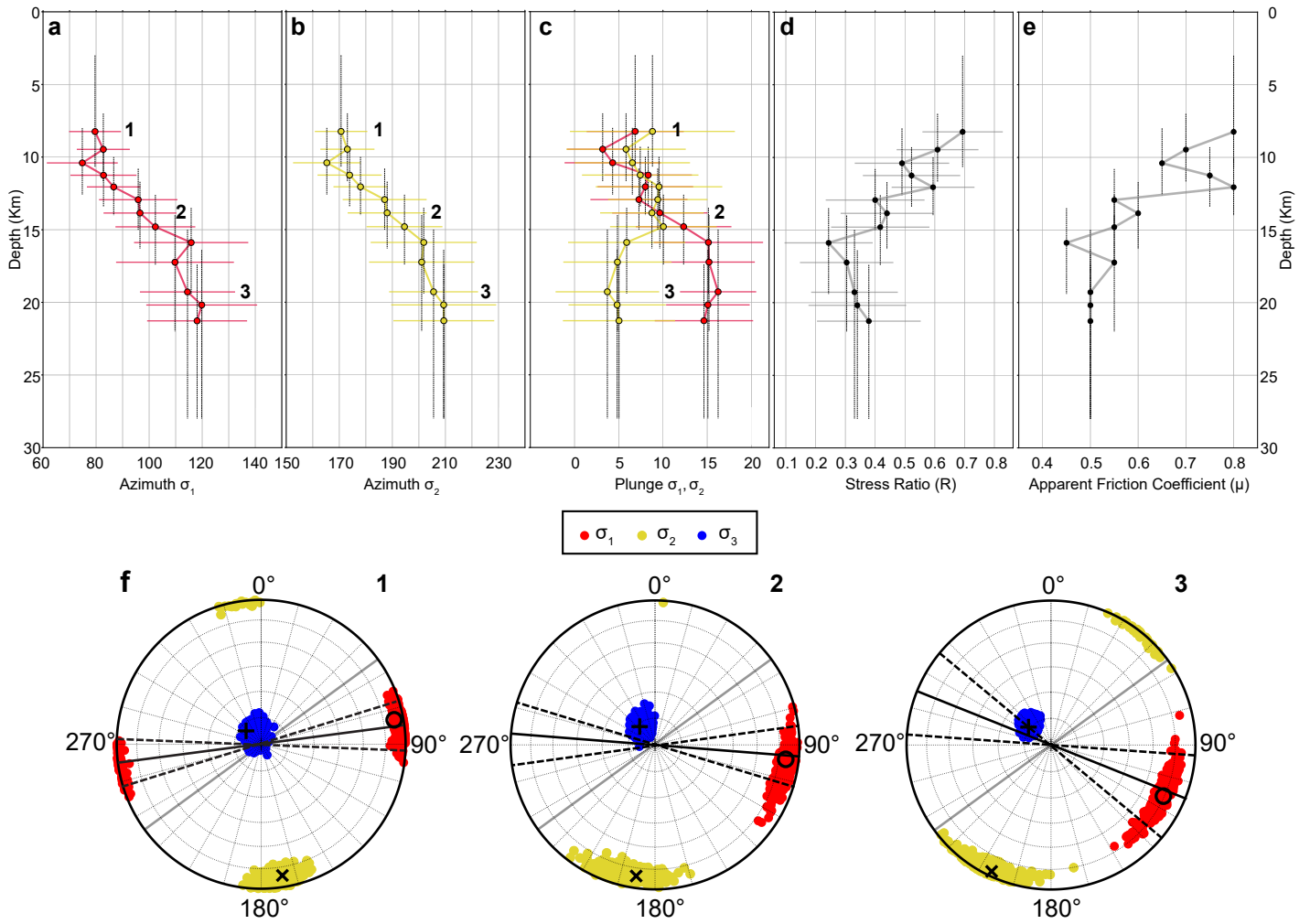


Figure 3. Depth-dependent variation of (a) σ_1 azimuth, (b) σ_2 azimuth, (c) σ_1 and σ_2 plunge, (d) stress ratio, and (e) apparent friction coefficient in moving windows of 75 events, overlapping by 15 events. Vertical lines represent depth range of the FMS used in each window, horizontal lines indicate 95% confidence interval. (f) Polar plots of specific stress inversions denoted by numbers (1-3). Black solid lines represent the orientation of the maximum horizontal stress (SHmax), with black dashed lines indicating 95% confidence interval limits of the. Grey solid lines represent the SHmax orientation from borehole breakouts (Mazzotti & Townend, 2010).

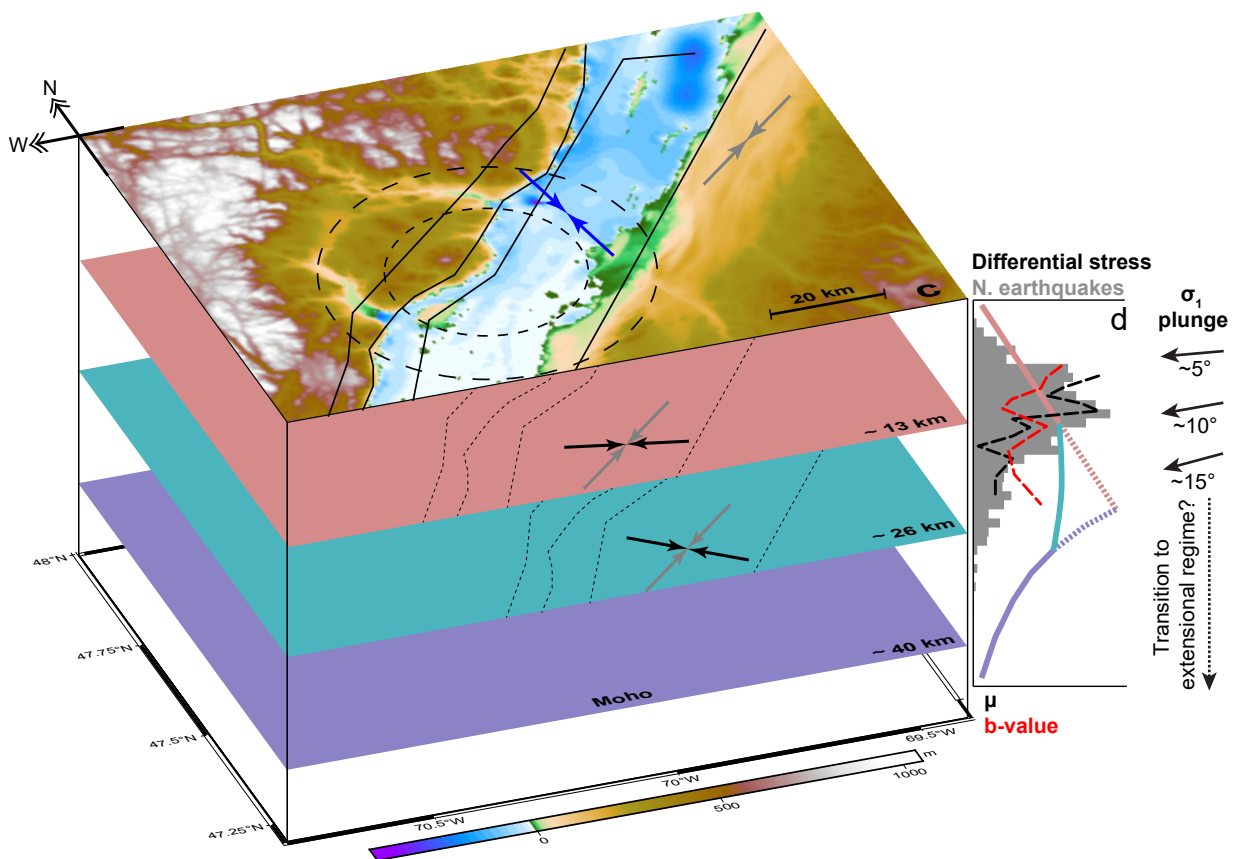
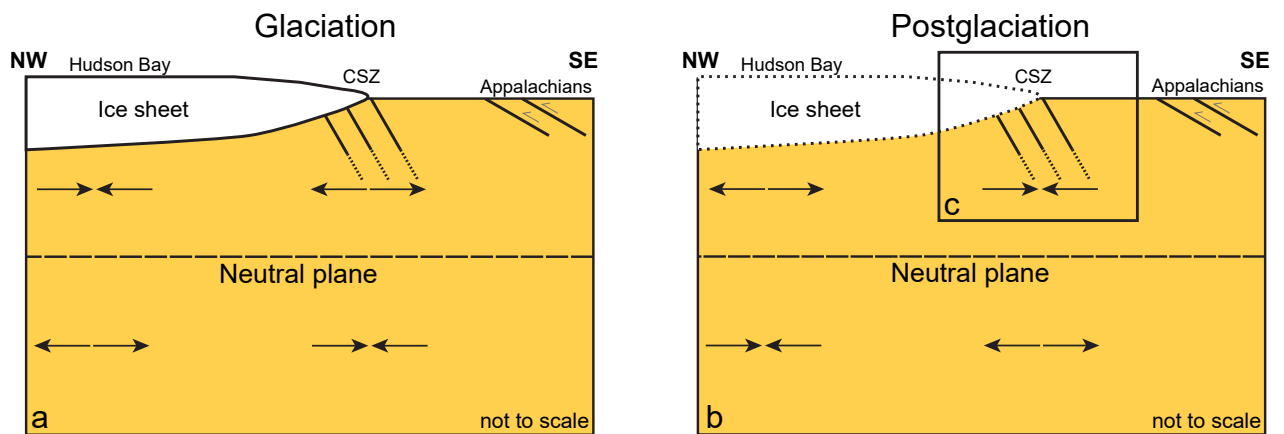


Figure 4. Schematic NW-SE cross section showing the expected horizontal stress distribution in the lithosphere during (a) glacial loading and (b) postglacial unloading following Wisconsin glaciation (85-11 kyr). (c) Conceptual model showing crustal depth-dependent clockwise rotation of maximum horizontal stress (S_{Hmax}) in the CSZ calculated here (black arrows) compared to S_{Hmax} from borehole breakouts data (grey arrows), and maximum horizontal strain direction from GIA modeling (Peltier et al., 2015). (d) Hypothetical rheological profile of the crust (solid lines color-coded by section of the crust) in the CSZ based on the distribution of earthquakes (grey histogram), b-value (dashed red line), apparent friction coefficient (μ) (dashed black line). Black arrows show the calculated rotation of the σ_1 plunge interpreted as possible transition to an extensional regime approaching the neutral plane (a, b). Vertical and horizontal axis do not have the same scale.